EUROPEAN JOURNAL OF MATERIALS SCIENCE AND ENGINEERING
Volume 11, Issue 1, 2026: 51-58 | www.ejmse.ro | ISSN: 2537-4338

EJMSE

DOI: 10.36868/ejmse.2026.11.01.051

STRUCTURAL OPTICAL AND PHOTODEGRADATION PROPERTIES OF NANOSTRUCTURED $BiFeO_3$ COMPOUND

Mayuri CHOUREY[1][0009-0005-0802-0940], Aditya Narayan BHATT[1][0000-0003-4525-2482]

[1]School of Engineering & Technology, Department of Mechanical Engineering, Sanjeev Agrawal Global Education (SAGE) University, Bhopal-462022, India

Abstract

This study presents a novel exploration into the photocatalytic properties of nanostructured $BiFeO_3$, synthesized using the ultrasonication-assisted sol-gel technique. Rietveld-fittedX-ray diffraction studies reveal that the synthesized compoundexhibits rhombohedralsymmetry (R3c space group).The scanning electron microscopy (SEM) analysis shows that the particles have a spherical shape with a flake-like grain structure. The particle size distribution, determined from the SEM images, is around 23.75 nm.The FTIR and Raman spectra confirmed the mono-phase composition.Optical properties, examined through UV-Vis spectroscopy, direct energy band gap of 2.216 eV. To further assess the photocatalytic activity of $BiFeO_3$, the degradation of Methylene Blue (MB) was investigated under visible light, resulting in an impressive efficiency of 98%.

Keywords: *$BiFeO_3$, X-ray diffraction, Band Gap, Photodegradation, Methylene Blue*

Introduction

In recent years, nanostructured materials, with their unique properties distinct from their bulk counterparts, have shown immense potential for advanced technological applications, particularly in the field of photocatalysis [1-3]. Among these, iron-based perovskites, typically represented by the formula $AFeO_3$ (where A denotes metal ions such as Ca, Sr, Ba, Bi, La, Gd, Ga, or Y), have gained significant attention for their multifunctional characteristics [4, 5]. When synthesized at the nanoscale, these materials can incorporate both magnetism and ferroelectricity, which enhance their photocatalytic performance for photodegradation processes. Magnetism facilitates the efficient recovery of photocatalysts using external magnetic fields, while ferroelectricity aids in the effective separation of photogenerated charge carriers, thus preventing recombination and boosting catalytic efficiency [6]. Ferroelectric materials are highly sought after for their intrinsic polarization, which inhibits the recombination of photon-induced electron-hole pairs, making them ideal for degrading a variety of pollutants, including CO_2, CO, methylene blue (MB), and other organic contaminants [7]. Multifunctional oxides, such as TiO_2, WO_2, SnO_2, Fe_2O_3, and ZnO [8-12], have also been widely studied for photocatalytic applications. However, their relatively large optical bandgap (>3 eV) limits their efficiency under visible light, highlighting the potential of materials that can utilize the entire solar spectrum for enhanced degradation processes.

$BiFeO_3$, a multiferroic compound with a low optical bandgap (Eg~2.2 eV) and a high polarisation value (100 C/cm^2), emerges as a promising choice. $BiFeO_3$ (BFO) structure is Rhombohedral distorted perovskite with R3c space group [13]. The stereochemical activity of the 6s2 electron lone pair of Bi^{3+} causes a cationic shift in the crystal, resulting in room-temperature ferroelectric behavior [14]. The immense potential applications of these findings in photocatalysis and environmental remediation are a beacon of hope, inspiring further research and development.

*Corresponding author: mayurichourey14@gmail.com

© 2026 The Author(s). OPEN ACCESS: CC BY-NC license http://creativecommons.org/licenses/by-nc/4.0/

However, numerous studies have focused on enhancing the visible-light-driven photocatalytic activity of transition metal-doped $BiFeO_3$ compounds [15]. Wang et al. reported that Oxygen vacancies induced by zirconium doping in bismuth ferrite nanoparticles for enhanced photocatalytic performance [16]. Furthermore, Meng et al. investigated the influence of lanthanum doping on the photocatalytic properties of $BiFeO_3$ for phenol degradation [17]. Similarly, Dhanalakshmi et al. reported enhanced photocatalytic activity in La-substituted BiFeO3 nanostructures for the degradation of phenol red [18]. Additionally, Esmaili et al. successfully demonstrated the impact of Nd and Zr co-substitution on the structural, magnetic, and photocatalytic properties of $Bi_{1-x}Nd_xFe_{1-x}Zr_xO_3$ nanoparticles [19]. Beyond these studies, numerous approaches have been explored to improve photocatalytic activity, including doping with other elements, forming composites, and optimizing synthesis methods. Earlier studies focused on improving $BiFeO_3$'s multiferroic and magnetoelectric properties, but it also shows great potential for photocatalytic applications. Various synthesis methods have enhanced its magnetoelectric and optical properties. Xian et al. reported improved photocatalytic performance of BiFeO3with reduced particle size [20]. While BFO has been synthesized via solid-state and wet chemical methods, high-temperature synthesis lowers its photocatalytic efficiency [21]. Motivated by this, we synthesized $BiFeO_3$ nanoparticles at low temperatures using an ultrasonication-assisted sol-gel method and explored their enhanced optical properties.

In this study, considering the above factors, we successfully synthesized uniform nanoparticles of $BiFeO_3$ using a conventional ultrasonication-assisted sol-gel method. We further investigated the structural, optical, and photodegradation properties of the nanostructured $BiFeO_3$ compound.

Experimental Procedure

Nanostructured BFO was synthesized using an ultrasonication-assisted sol-gel technique, following procedures similar to those outlined in previous studies [22-24]. High-purity analytical-grade chemicals were used, including bismuth nitrate pentahydrate [$Bi(NO_3)_3 \cdot 5H_2O$], iron (III) nitrate nonahydrate [$Fe(NO_3)_3 \cdot 9H_2O$], and tartaric acid [$C_4H_6O_6$], all without further purification. Double-distilled water was employed throughout the entire process.

Bismuth nitrate pentahydrate [$Bi(NO_3)_3 \cdot 5H_2O$] and iron (III) nitrate nonahydrate [$Fe(NO_3)_3 \cdot 9H_2O$] was dissolved in double-distilled water in a 1:1 ratio, followed by ultrasonication for 2 hours. Tartaric acid was added as a complexing agent (2 mol per 1 mol of metal ions) to prevent aggregation and promote uniform particle formation. The solutions were combined, and the pH was adjusted to 1 with nitric acid. The mixture was ultrasonicated for 3 hours, resulting in a yellow gel, which was dried at 363 K. The powder was then calcined at 873 K for 2 hours and sintered into pellets at the same temperature for 2 hours in ambient air.

The crystal structure of BFO was analyzed using X-ray diffraction (Cu-Kα radiation) on a Bruker D-8 Advance diffractometer and refined with Fullprof software. FTIR analysis confirmed key chemical bonds in the compound using a Bruker Vertex 70 spectrometer. UV-vis absorption spectra were recorded with a Rigol Ultra 3660 spectrophotometer. The photocatalytic activity of BFO was tested for MB degradation under visible light using a 150W xenon lamp (400 nm). A 10 mg/L catalyst was used in a 10 ppm MB solution, with absorbance monitored at 556 nm.

Results and Discussions

The Rietveld refinement of X-ray diffraction (XRD) data for $BiFeO_3$ synthesized via ultrasonication-assisted sol-gel method is shown in Fig. 1(a). The Bragg peaks confirm the compound's rhombohedral structure with an R3c space group. The single-phase nature of the compound is verified by the consistent indexing of all characteristic peaks with theoretical data, with no evidence of secondary or impurity phases. The refinement process began by adjusting the scale and zero factors, followed by the determination of lattice constants. The full-width at

half-maximum (FWHM) and background parameters were refined individually, while atomic positions were adjusted relative to isotropic factors. The fitting continued until the reliability factors reached acceptable values (χ^2 = 1.3). The Wyckoff positions of the constituent elements are as follows: Bi at 6a (0, 0, z), Fe at (0, 0, 0), and O at 18b (x, y, z) [22, 23]. Fig. 1(a) clearly shows peak broadening at the base, indicating reduced crystallinity and confirming the nanocrystalline nature of the material. Refined parameters, including atomic positions, occupancy, bond lengths, and bond angles, are listed in Table 1. Using these parameters, the crystal structure was modeled using VESTA software, with the inset of Fig. 1(a) visually representing the octahedral distortions.

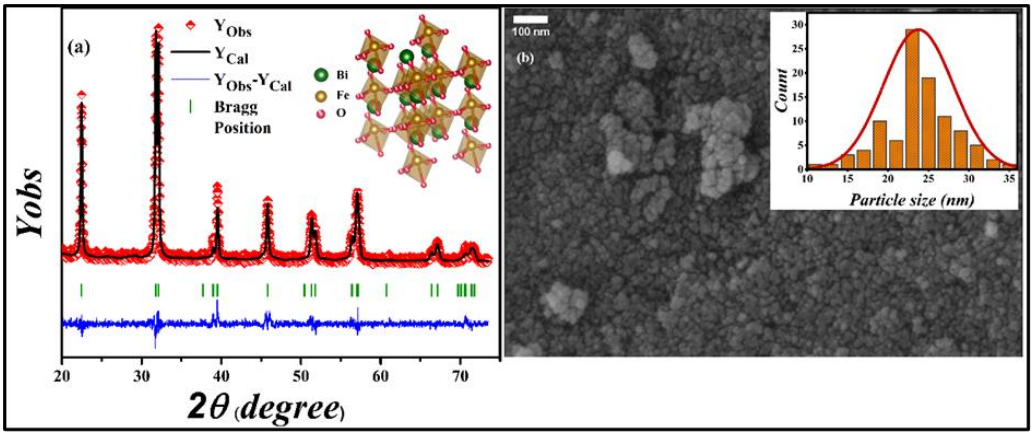

Fig. 1. (a) Room temperature XRD and (b) SEM image of $BiFeO_3$

Scanning Electron Microscopy (SEM) images, shown in Fig. 1(a-c), were used to investigate the surface morphology and grain distribution of the reported compounds. The images reveal spherical, agglomerated, and irregularly shaped particles with voids and pores, indicating the release of gases such as carbon dioxide and nitrogen during the combustion process [4, 22]. The grain size histogram, presented in the inset of the representative SEM images, shows that the average grain size for the composition is 23.75 nm.

Fig. 2(a) displays the Fourier-transform infrared (FTIR) spectra of $BiFeO_3$ in the 400 to 4000 cm^{-1} range, providing insight into its molecular bonding. Within the 400 cm^{-1} to 600 cm^{-1} range, distinct peaks are observed, corresponding to the stretching and vibrational modes of metal-oxide bonds. These peaks are linked to the characteristic FeO_6 and BiO_6 octahedral configurations, confirming the formation of BFO [25]. Specifically, peaks at 426 cm^{-1} and 440 cm^{-1}, shown in the inset of Fig. 2(a), are attributed to the bending vibrations of Bi-O-Bi and Fe-O-Fe bonds, respectively [26]. The broad peak at 550 cm^{-1} results from the overlap of Bi-O and Fe-O stretching vibrations [27]. Additionally, other peaks in the spectrum suggest the presence of functional groups, as indicated in Fig. 2(a) [28]. This detailed analysis of the FTIR spectra provides valuable information on the molecular composition and bonding characteristics of BFO synthesized via the ultrasonication-assisted sol-gel method.

Fig. 2(b) presents the Raman spectra of $BiFeO_3$ in the range of 50 to 750 cm^{-1}, revealing several molecular interactions. According to group theory, it exhibits 13 Raman-active modes, as described by Γ_{Raman}, R3c = 4A1 + 9E [29]. The 4A1 and 9E modes correspond to the transverse and longitudinal optical modes, polarized along the z-axis and x-y plane, respectively. The spectra were further deconvoluted into individual Raman modes: A_{11}(138), A_{12}(171.67), A_{13}(221.38), E_1(73), E_3(253.81), E_4(293.61), E_5(336.19), E_6(360.89), E_7(470.41), E_8(530.22), and E_9(579.04). These modes are consistent with those reported by Kothari et al. [30]. The intensity differences between the A_1 and E modes arise from the unpolarised measurement condition. The presence of

lone pair electrons in Bi^{3+} ions leads to stereochemical activity in Bi-O bonds, which influences ferroelectricity and polarizability, resulting in six low-frequency Raman-active modes: E_1, E_2, A_{11}, A_{12}, A_{13}, and A_{14} [31]. In this study, E_1, A_{11}, A_{12}, and A_{13} are observed. The moderate-frequency modes E_3 and E_4 correspond to Fe-O bonds, while the higher-frequency modes E_5 to E_9 are attributed to vibrations of Fe in FeO_6 octahedral [32].

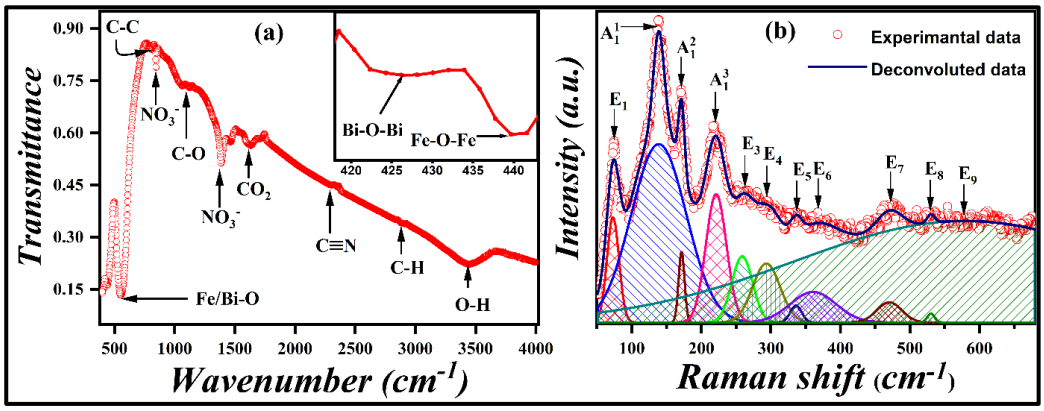

Fig. 2. (a) FTIR and (b) Raman spectra of $BiFeO_3$

The optical properties of a compound provide valuable insights into its electronic transition levels. To explore this, UV-visible spectroscopy was performed in the 300 to 800 nm range, as shown in Fig. 3(a). The absorption spectrum displays a broad feature in the visible region, with a distinct absorption peak observed at 560 nm. The energy band gap was determined using the modified Tauc's relation [33], as expressed below:

$$(\alpha h\nu)2 = \beta(h\nu - Eg) \quad (1)$$

In this equation, α represents the absorption coefficient, h is Planck's constant, ν is the frequency of the incident radiation, β is the band tailing parameter, and n defines the nature of the optical band gap. When n = 1/2, the band gap is indirect, and when n = 2, it is direct. Based on previous studies, it is known to have a direct optical band gap [34]. By performing a linear fit of the absorption data, the direct optical band gap was calculated to be 2.216 eV, as shown in Fig. 3(a).

The electronic structure is characterized by O-2p and Bi-6s orbitals in the valence band and Fe-3d and Bi-6p orbitals in the conduction band. Crystal field splitting causes the octahedral t2g3eg2 configuration to transform into the rhombohedral $a_1^1e^2e^2$ configuration. This results in hybridized O-2p and Fe-3d (a11) states in the valence band, just below the Fermi level, and hybridized O-2p, Fe-3d (e2), and Bi-6p states in the conduction band at higher energies. These interactions lead to various inter-atomic transitions, including the Fe 3d-d absorption band, which is attributed to the electron spin in the Fe 3d5 state, as observed in prior studies [34, 35]. The main optical transitions are attributed to interatomic O-2p ↔ Fe-3d transitions and intra-atomic Fe d-d transitions.

To assess the photodegradation performance, 10 mg of $BiFeO_3$ nanoparticles were suspended in 100 mL of a 10 mg/L MB (Methylene Blue) aqueous solution. The mixture was stirred in the dark to allow the system to reach adsorption-desorption equilibrium. Subsequently, the mixture was exposed to light from a tungsten lamp (λ > 400 nm) for various time intervals. Fig. 3(b) illustrates the photodegradation of MB, showing the process at the initial time of 0 minutes and after 270 minutes, with intermediate time points included. The degradation efficiency was calculated using the following mathematical equation [36]:

$$\left\{\frac{C_0 - C}{C_0} \times 100\right\} \quad (2)$$

Where C_0 is the initial concentration and C is the concentration at a given time.

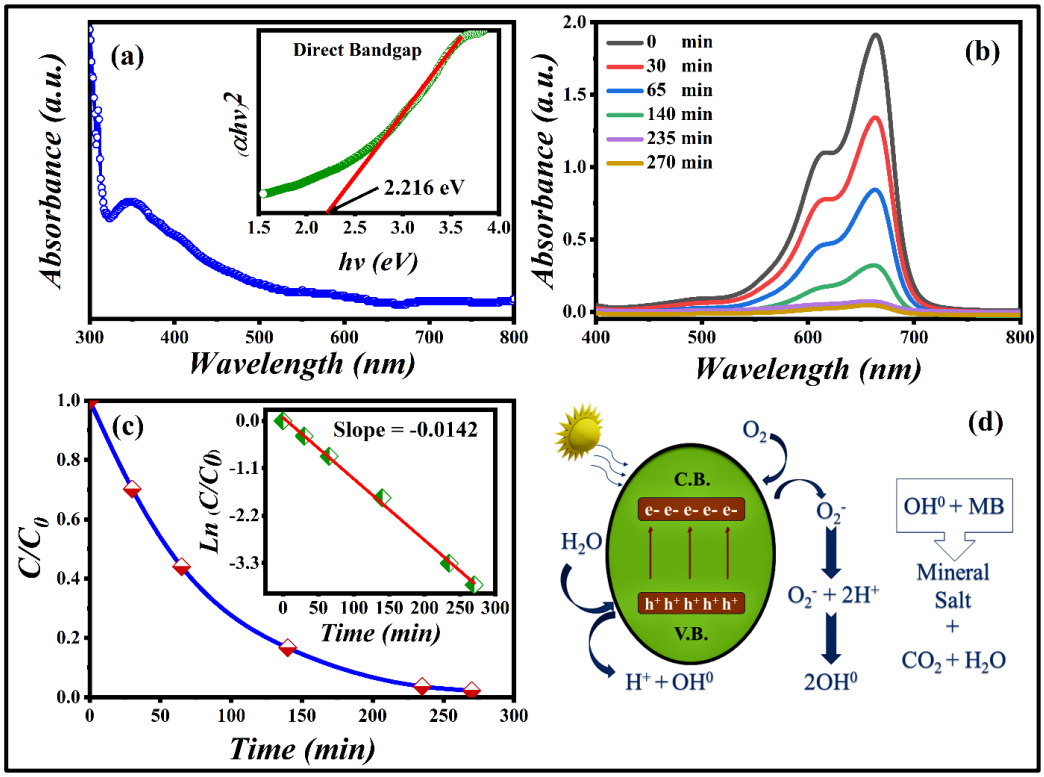

Fig. 3. (a) UV-Vis spectra of BFO with Tauc plot in inset (b) Photodegradation graph of MB using BFO as Photocatalyst (c) Degradation concentration with varying time along with reaction kinetic in inset (d) Schematic representation of Photocatalytic reaction

Fig. 3(c) illustrates the degradation rate as a function of time. The MB degradation rates observed at different time intervals are 30%, 56%, 83%, 96%, and 98% after 30, 65, 140, 235, and 270 minutes, respectively. The degradation rate constant is determined using pseudo-first-order reaction kinetics, as shown below [37]:

$$ln\frac{C}{C_O} = -kt \quad (3)$$

Where C_0 represents the initial MB concentration, C is the concentration at time t, and k is the degradation rate constant. The degradation rate constant, determined by the linear fitting of ln (C/C_0) vs. time (t)was found to be 0.0142 min^{-1}. The possible mechanism for the degradation of MB using nanoparticles is illustrated in Fig. 4(d). Upon irradiation with visible light, electrons are excited from the valence band to the conduction band, leaving behind holes. The nanoparticles actively participate in redox reactions on their surface with the separated electrons and holes. The electrons are absorbed by O_2 molecules, while the holes interact with H_2O molecules, resulting in the formation of active OH^-* and O_2^-* radicals. The equations for the formation of these radicals are as follows [38]:

$$BiFeO_3 + h\nu \rightarrow BiFeO_3^* + e^- + h^+ \quad (4)$$
$$H_2O + h^+ \rightarrow OH^- + H^+ \quad (5)$$
$$h_{VB}^+ + H_2O \rightarrow OH^{-*} + H^+ \quad (6)$$
$$e_{CB}^- + O_2 \rightarrow O_2^{-*} \quad (7)$$
$$MB\ (dye) + O_2^{-*} + OH^{-*} \rightarrow Products \rightarrow H_2O + CO_2 \quad (8)$$

The involvement of reactive oxygen species (ROS), such as superoxide radicals (O_2^-) and hydroxyl radicals (OH^-), plays a crucial role in influencing photocatalytic activity, driving and enhancing the overall efficiency of BFO photocatalysts [38]. Previous studies have reported relatively lower degradation efficiency under visible light irradiation for various inorganic dyes [39, 40]. However, the ultrasonication-assisted sol-gel method used in this study is of critical importance, as it results in a smaller grain size (~23.75 nm) and a uniform particle size distribution, thereby significantly improving photodegradation performance under visible light irradiation.

Table 1. Atomic positions and bond parameters were calculated from Rietveld refinement of the X-ray diffraction pattern

Atom	Wyckoff	X	Y	Z	Occupancy
Bi^{+3}	6a	0.00000	0.00000	0.72713	0.34354
Fe^{+3}	6a	0.00000	0.00000	0.00000	0.34347
O^{-2}	18b	0.85593	0.65897	0.48414	0.90897
Bond length (in Å)			**Bond angle (in degree)**		
Fe-O	2.6184		Fe-O-Fe	157.437	
Bi-O	3.1897		Bi-O-Bi	148.076	

As discussed earlier, during the photocatalytic degradation of organic dyes, the migration of photoexcited electrons and holes to the photocatalyst surface is essential to prevent their recombination. Smaller particles reduce the distance between the photoexcited carriers and the $BiFeO_3$/dye interface, which in turn lowers the recombination rate of holes and electrons [41, 42]. Consequently, the enhanced photocatalytic performance of BFO synthesized via the ultrasonication-assisted sol-gel method can be attributed to the smaller grain size and altered morphology, which facilitate improved charge separation and transport at the $BiFeO_3$/dye interface.

Conclusions

Our study provides a thorough characterization of $BiFeO_3$ (BFO) synthesized via the ultrasonication-assisted sol-gel method, employing a multi-technique approach. Rietveld refinement of XRD data, in conjunction with SEM analysis and particle size determination, confirms the single-phase formation, nanocrystalline structure, and uniform grain distribution of the material, offering valuable insights into its structural and morphological properties. FTIR analysis reveals the presence of metal oxide bonds and functional groups, supporting phase formation, while RAMAN spectroscopy identifies key molecular interactions and active Raman modes, particularly those associated with Bi-O and Fe-O bonds. The optical properties indicate a direct bandgap of 2.216 eV. Notably, the photocatalytic performance of the synthesized BFO was evaluated through methylene blue (MB) degradation, demonstrating remarkable efficiency with nearly 98% dye degradation without requiring additional reagents. This comprehensive characterization highlights the potential of the ultrasonication-assisted sol-gel method for producing BFO with excellent structural, morphological, and photocatalytic properties, paving the way for its application in environmental remediation and energy conversion processes.

Acknowledgments / Funding body

The authors also acknowledge Dr. Mukul Gupta (UGC-DAE CSR Indore) for providing measurement facilities.

Credit author statement

Mayuri Chourey: Conceptualization, Methodology, Experimentation, Original draft, Writing, Editing; Aditya Narayan Bhatt: Reviewing and Editing

References

[1] M B. Zaman, R. Poolla, S. A. Khandy, A. Modi, R. K. Tiwari, Nanotech. 32 (2021) 245706, https://doi.org/10.1088/1361-6528/abec09.
[2] R. A. Parry, K. Dubey, A. Modi, N. K. Gaur, Results in Optics 16 (2024) 100677, https://doi.org/10.1016/j.rio.2024.100677.
[3] A. A. AlObaid, G. Nazir, A. Modi, S. Thakur, J. H. Malik, Inorg. Chem. Commun.161 (2024) 112060, https://doi.org/10.1016/j.inoche.2024.112060.
[4] R. Yadav, A. Modi, K. Dubey, M. M. Malik, J Mater Sci: Mater Electron 34 (2023) 1243, https://doi.org/10.1007/s10854-023-10630-4.
[5] T. Bagwaiya, H. A. Reshi, P. Khade, S. Bhattacharya, V. Shelke, J. Magn. Magn. Mater. 483 (2019) 59-64, https://doi.org/10.1016/j.jmmm.2019.03.092.
[6] R. Aswini, S. Hartati, K. Jothimani, R. Pothu, P. Shanmugam, Y. Lee, S. Masimukku, R. Boddula, M. Selvaraj, N. Al-Qahtani, J. Environ. Manag. 370 (2024) 122738, https://doi.org/10.1016/j.jenvman.2024.122738.
[7] E. A. Volnistem, R. D. Bini, G. S. Dias, L. F. Cótica and I. A. Santos, *Ferroelectrics* 534 (2018) 190-198, https://doi.org/10.1080/00150193.2018.1473675.
[8] Chen Xu, G. P. Rangaiah, X. S. Zhao, Ind. Eng. Chem. Res. 53(38) (2014) 14641-14649, https://doi.org/10.1021/ie502367x.
[9] R. A. Parry, K. Dubey, A. Modi, N. K. Gaur, Results Opt. 16 (2024) 100677, https://doi.org/10.1016/j.rio.2024.100677.
[10] D. Majumder, I. Chakraborty, K. Mandal, S. Roy, ACS Omega4(2) (2019) 4243-4251, https://doi.org/10.1021/acsomega.8b03298.
[11] M. B. Goudjila, H. Dalia, S. Zighmib, Z. Mahcenec, S. E. Bencheikh, Desalin. Water. Treat.317 (2024) 100079,https://doi.org/10.1016/j.dwt.2024.100079.
[12] S. Yadav, J. Jindal, A. Mittal, S. Sharma, K. Kumari, N. Kumar, J. Phys. Chem. Solids.157 (2021) 110217, https://doi.org/10.1016/j.jpcs.2021.110217.
[13] S. Chauhan, M. Kumar, P. Pal, RSC Adv.6 (2016) 68028-68040,https://doi.org/10.1039/C6RA11021E.
[14] L.W. Martin, Dalton Trans. 39 (2010) 10813-10826,https://doi.org/10.1039/C0DT00576B.
[15] G. Huang, G. Zhang, Z. Gao, J. Cao, D. Li, H. Yun, T Zeng, J. Alloys Compd. 783 (2019) 943-951, https://doi.org/10.1016/j.jallcom.2019.01.017.
[16] F. Wang, D. Chen, N. Zhang, S.Wang, L. Qin, X. Sun, Y. Huang, J. Colloid Interface Sci. 508 (2017) 237-247, https://doi.org/10.1016/j.jcis.2017.08.056.
[17] W. Meng, R. Hu, J. Yang, Y. Du, J. Li, H. Wang, Chin. J. Catal. 37(8) (2016) 1283-1292,https://doi.org/10.1016/S1872-2067(16)62449-X.
[18] R. Dhanalakshmi, M. Muneeswaran, K. Shalini, N.V. Giridharan, Mater. Lett. 165 (2016) 205-209, https://doi.org/10.1016/j.matlet.2015.11.106.
[19] L. Esmaili, A. Gholizadeh, Mater. Sci. Semicond. Process. 118 (2020) 105179, https://doi.org/10.1016/j.mssp.2020.105179.

[20] T. Xian, H. Yang, J.F. Dai, Z.Q. Wei, J.Y. Ma, W.J. Feng, Mater. Lett. 65(11) (2011) 1573-1575, https://doi.org/10.1016/j.matlet.2011.02.080.
[21] L. Wang, J. Xu, B. Gao, A. Chang, J. Chen, L. Bian, C. Song, Mater. Res. Bull. 48(2) (2013) 383-388, https://doi.org/10.1016/j.materresbull.2012.10.038.
[22] P. Joshi, A. Modi, S. K. Kapoor, S. Tiwari, J. Shukla, A. Mishra, J Mater Sci: Mater Electron 34 (2023) 1783, https://doi.org/10.1007/s10854-023-11202-2.
[23] P. Joshi, A. Modi, S. K. Kapoor, S. Tiwari, J. Shukla, Ashutosh Mishra, J Mater Sci: Mater Electron 35 (2024) 1946, https://doi.org/10.1007/s10854-024-13740-9.
[24] A. Mukherjee, S. Basu, P.K. Manna, S. M. Yusuf, M. Pal, Journal of Alloys and Compounds 598 (2014) 142–150, http://dx.doi.org/10.1016/j.jallcom.2014.01.245.
[25] H. Maleki, J. Mater. Sci. Mater. Electron. 29 (2018) 11862–11869. https://doi.org/10.1007/s10854-018-9286-7.
[26] F. Bhadala, L. Suthar, P. Kumari and M. Roy, Mater. Chem. Phys. 247 (2020) 122719. https://doi.org/10.1016/j.matchemphys.2020.122719.
[27] M. Nadeem, W. Khan, S. Khan, M. Shoeb, S. Husain and M. Mobin, Mater. Res. Express 5 (2018) 065506. https://doi.org/10.1088/2053-1591/aac70d.
[28] V. M. Gaikwad and S. A. Acharya, J. Appl. Phys. 114, (2013), 193901. http://dx.doi.org/10.1063/1.4831676.
[29] M. Muneeswaran, R. Dhanalakshmi and N.V. Giridharann, Ceram. Int. 41 (2015) 8511-8519. http://dx.doi.org/10.1016/j.ceramint.2015.03.058.
[30] D. Kothari, V.R. Reddy, V.G. Sathe, A. Gupta, A. Banerjee, A.M. Awasthi, J. Magn. Magn Mater. 320 (2008) (3–4) 548–552. https://doi.org/10.1016/j.jmmm.2007.07.016.
[31] P. Pandit, S. Satapathy, P. K. Gupta and V. G. Sathe, J. Appl. Phys. 106 (2009) 114105). http://dx.doi.org/10.1063/1.3264836.
[32] S.R. Dhanya, S.G. Nair, J. Satapathy and N.P. Kumar, AIP Conf Proc. 2166 (2019) 020017. https://doi.org/10.1063/1.5131604.
[33] D. K. Pandey, A. Modi, P. Pandey, N.K. Gaur, J. Mater. Sci. Mater. Electron., 28 (22) (2017) 17245–17253, https://doi.org/10.1007/s10854-017-7655-2.
[34] X. Bai, J. Wei, B. Tian, Y. Liu, T. Reiss, N. Guiblin, P. Gemeiner, B. Dkhil and I. C. Infante, J. Phys. Chem. C 120 (2016) 3595–3601. https://doi.org/10.1021/acs.jpcc.5b09945.
[35] H. Wang, Y. Zheng, M.Q. Cai, H. Huang and H.L.W. Chana, Solid State Commun. 149 (2009) 641-644. https://doi.org/10.1016/j.ssc.2009.01.023.
[36] X. Wang, Y. Lin, X. Ding, Jinguo Jiang, J. Alloys Compd 509 (2011) 6585–6588, https://doi.org/10.1016/j.jallcom.2011.03.074.
[37] H. Azmy, N. Razuki, A. Aziz, N. Satar, N. Kaus, J. Phys. Sci., 28(2) (2017) 85–103, https://doi.org/10.21315/jps2017.28.2.6.
[38] T. Cadenbach, M. J. Benitez, A. L. Morales, C. C. Vera, L. Lascano, F. Quiroz, A. Debut, K. Vizuete, Beilstein J. Nanotechnol. 11 (2020) 1822–1833, https://doi.org/10.3762/bjnano.11.164.
[39] X. Wang, W. Mao, Q. Zhang, Q. Wang, Y. Zhu, J. Zhang, T. Yang, J. Yang, X.'a. Li, W. Huang, J. Alloys and Compd. 677 (2016) 288-293.
[40] T. Gao, Z. Chen, Y. Zhu, F. Niu, Q. Huang, L. Qin, X. Sun, Y. Huang, Mater. Res. Bull. 59 (2014) 6–12.
[41] G.M. Wang, Y.C. Ling, D.A. Wheeler, K.E.N. George, K. Horsley, C. Heske, J.Z. Zhang, Y. Li, Nano Lett. 11 (2011) 3503–3509.
[42] J. He, R. Guo, L. Fang, W. Dong, F. Zheng, M. Shen, Mater. Res. Bull. 48 (2013) 3017–3024.

Received: October 02, 2025
Accepted: February 12, 2026